Radiometric Correction of Airborne Radar Images Over Forested Terrain With Topography

Marc Simard, Bryan V. Riel, Michael Denbina, and Scott Hensley

***Abstract*—Radiometric correction of radar images is essential to produce accurate estimates of biophysical parameters related to forest structure and biomass. We present a new algorithm to correct radiometry for 1) terrain topography and 2) variations of canopy reflectivity with viewing and tree-terrain geometry. This algorithm is applicable to radar images spanning a wide range of incidence angles over terrain with significant topography and can also take into account aircraft attitude, antenna steering angle, and target geometry. The approach includes elements of both homomorphic and heteromorphic terrain corrections to correct for topographic effects and is followed by an additional radiometric correction to compensate for variations of canopy reflectivity with viewing and tree-terrain geometry. The latter correction is based on lookup tables and enables derivation of biophysical parameters irrespective of viewing geometry and terrain topography. We evaluate the performance of the new algorithm with airborne radar data and show that it performs better than classical homomorphic methods followed by cosine-based corrections.**

***Index Terms*—Biomass, forest, radar, radiometric correction, topography.**

I. INTRODUCTION

RADIOMETRIC calibration of synthetic aperture radar (SAR) data has been an ongoing issue for several decades. While a wealth of SAR data is now available, the distributed data sets are seldom corrected for the impact of terrain topography on the radar backscatter. Terrain topography is responsible for most of the radiometric variations observed in SAR images, making the retrieval of biophysical parameters from radar backscatter only possible on relatively flat terrain, or after correction of the topographic effects [1]–[5]. Although a few commercial and public software programs enable users to perform correction through the use of external digital elevation models (DEMs), every software, to our knowledge, bases the correction on the local incidence angle only. Radiometric corrections based on local incidence angle alone can be sufficient over relatively flat terrain and within a limited range of incidence angles; however, they do not work well in areas with significant topographic features, where many of the assumptions of their simplified models are no longer valid [6].

In this paper, we compare several methods and demonstrate our new approach using UAVSAR, which is an airborne L-band polarimetric SAR with look angles varying between about 20° and 70°. The UAVSAR radar antenna is electronically steered to compensate for aircraft attitude such that the zero Doppler point is located at boresight (45°) perpendicular to the flight track (i.e., broadside).

In Section II, we discuss three different methods for radiometric calibration based on area projection. Following these area normalization methods, we discuss radiometric correction due to changes in the reflectivity of the target as a function of viewing and terrain geometry in Section III and introduce a new method, performed after area normalization, designed for the radiometric correction of forested surfaces. Finally, we conclude in Section IV.

II. ILLUMINATED AREA PROJECTION

Several different radiometric calibration approaches persist in the scientific literature. The general approach, which is common to all methods, is to estimate the local ground area illuminated by the radar beam and normalize the radar backscatter values by an area factor, i.e.,

$$\sigma^\circ = \beta^\circ \frac{A_{\text{ref}}}{A} \tag{1}$$

where σ° is the calibrated backscatter value, β° is the uncorrected value, A_{ref} is the area of a radar pixel in the slant plane, and A is the illuminated ground area for that pixel. The method to estimate the local illuminated area can be done through 1) estimation of the local incidence angle or some other projection angle [7] or 2) integration of the DEM [6] and [8]. The former method has the advantage of being simpler to implement, whereas the latter is more accurate, particularly in steep terrain, but is more computationally intensive. The integration involves determining the number of DEM pixels belonging to each radar range and azimuth pixel through knowledge of the geocoding process.

A. Homomorphic Calibration

Homomorphic calibration techniques assume a one-to-one transformation between the radar and map geometries (i.e.,

---

Manuscript received May 24, 2015; revised August 14, 2015, November 5, 2015, and February 11, 2016; accepted March 8, 2016. Date of publication April 5, 2016; date of current version June 1, 2016. This work was carried out at the Jet Propulsion Laboratory, California Institute of Technology, under a contract with the National Aeronautics and Space Administration (NASA). This work was supported by NASA's Terrestrial Ecology Program (WBS 281945.02.61.03.26).

M. Simard, M. Denbina, and S. Hensley are with the Jet Propulsion Laboratory, Pasadena, CA 91109 USA (e-mail: marc.simard@jpl.nasa.gov).

B. V. Riel is with the California Institute of Technology, Pasadena, CA 91125 USA.

Color versions of one or more of the figures in this paper are available online at http://ieeexplore.ieee.org.

Digital Object Identifier 10.1109/TGRS.2016.2543142

slant range and geographic coordinates). As correctly noted in [6] and [8], this is not necessarily a valid assumption under certain sensor viewing geometries as many map pixels may fall within the same radar pixels in an irreversible transformation. Homomorphic calibration is performed in map geometry using the local incidence or projection angle.

1) Homomorphic Calibration Using the Local Incidence Angle: The conventional method to estimate the illuminated area of a map pixel is to use the local incidence angle, which is the angle between the surface normal vector and the look vector to the sensor [3]. The surface normal is defined by the terrain slope, i.e., S, and aspect, i.e., S_a, which are calculated as [9]

$$S = \arctan\sqrt{f_x^2 + f_y^2} \tag{2}$$

$$S_a = 270^\circ + \arctan\left(\frac{f_y}{f_x}\right) - 90^\circ\frac{f_x}{|f_x|} \tag{3}$$

where f_x and f_y are the gradients along the W–E and N–S directions, respectively, and are calculated using a third-order finite difference with a 3 × 3 moving window. The local incidence is calculated as

$$\cos\theta_i = \sin(\theta_l)\sin(S)\cos(\phi - S_a) + \cos(\phi)\cos(S) \tag{4}$$

where θ_l and ϕ are the average elevation (i.e., look) and azimuth angles from the SAR sensor, respectively. Then, the ground-area-normalized backscatter value is

$$\sigma^\circ = \beta^\circ\sin\theta_i. \tag{5}$$

2) Homomorphic Calibration Using the Projection Angle: An improved homomorphic calibration technique makes use of the projection angle ψ, which is defined as the angle between the surface normal and the normal to the imaging plane [7]. It was shown in [7] that the local incidence angle area estimation is an approximation to the projection angle derived area. For the UAVSAR system and viewing geometry parameters, we use the radar SCH coordinate system, where $\hat{s}$ is the along-track direction, $\hat{h}$ points opposite the aircraft nadir direction, and $\hat{c}$ completes the right-handed system. The projection area is

$$A = \frac{\Delta\rho\Delta az}{\langle\hat{n}_\Sigma, \hat{n}_I\rangle} \tag{6}$$

where $\Delta\rho$ and Δaz are the range and azimuth resolutions, respectively. $\hat{n}_\Sigma$ and $\hat{n}_I$ are the unit normal vectors to the terrain and the radar imaging slant plane. The projection angle can be defined as

$$\cos\psi = \langle\hat{n}_\Sigma, \hat{n}_I\rangle. \tag{7}$$

To construct the unit normal to the terrain, the terrain slope must be broken into components along the range and azimuth directions [10], i.e.,

$$\tan\tau_\rho = \tan S\cos\left(S_a - (\text{HEAD} - 90^\circ)\right) \tag{8}$$

$$\tan\tau_s = \tan S\cos(S_a - \text{HEAD}) \tag{9}$$

where S is the ground slope, S_a is the aspect, HEAD is the aircraft heading, τ_ρ is the ground slope in the range direction, and τ_s is the ground slope in the azimuth direction. Then, the unit normal to the terrain is

$$\hat{n}_\Sigma = \frac{-1}{\sqrt{1 + \tan^2\tau_\rho + \tan^2\tau_s}}\begin{bmatrix}\tan\tau_s\\ \tan\tau_\rho\\ -1\end{bmatrix}. \tag{10}$$

The derivation for the unit normal to the radar imaging slant plane first involves deriving an expression for the unit look vector from the sensor to the ground target. It can be shown that the look vector has the following form [11]:

$$\begin{aligned}\hat{l}_s &= \sin\alpha\cos\theta_p\cos\theta_y\\ &\quad + \cos\alpha(\sin\theta_p\cos\theta_{\text{ih}}\cos\theta_y + \sin\theta_{\text{ih}}\sin\theta_y)\\ \hat{l}_c &= -\sin\alpha\cos\theta_p\sin\theta_y\\ &\quad + \cos\alpha\left(-\sin\theta_p\cos\theta_{ih}\sin\theta_y + \sin\theta_{ih}\cos\theta_y\right)\\ \hat{l}_h &= \sin\alpha\sin\theta_p - \cos\alpha\cos\theta_p\cos\theta_{ih}\end{aligned} \tag{11}$$

where θ_y and θ_p are the aircraft yaw and pitch angles, α is UAVSAR's azimuth electronic steering angle, and θ_{ih} is the incidence angle of a horizontal patch on the ground. Note that α is taken into account to compute the correct look vector and resulting projection angle. For sensors without steering angle, (11) simplifies with $\alpha = 0$. Finally, $\hat{n_I}$ can be computed as

$$\hat{n}_I = \hat{s}\times\hat{l}. \tag{12}$$

The projection angle method still suffers from the homomorphic assumption, but to mitigate its effect, we introduce a hybrid projection angle (HPA) approach. First, we generate an illuminated area *image A* in map coordinates using (6), which we resampled to the radar geometry using inverse distance weighting and through knowledge of the map coordinates and the sensor position. For UAVSAR, this involved the transformation between geographic latitude/longitude to the SCH system (see Section II-A2) using the coordinate reference frame quantities found in the annotation file (i.e., the UAVSAR ASCII header file distributed with the data). Finally, the radiometric correction in (1) is performed on the β° values in radar geometry.

B. Heteromorphic Calibration Using DEM Integration

A more accurate estimation of the illuminated area requires integration of the DEM [6]. The premise of this approach is to determine the number of DEM pixels that fall within each radar pixel by taking advantage of knowledge of the transformation between map and radar geometries. Thus, the ground area is integrated over the DEM, and no information is lost as in the case of the homomorphic assumption. For UAVSAR, the process begins by decomposing the DEM into facets and computing the fractional range and azimuth bin corresponding to each map facet [12]. Then, a bilinear weighting model is used to distribute the facet area over the appropriate radar pixels. The integer bounds in the radar image become

$$\begin{aligned} r_1 &= \text{floor}(r), \quad r_2 = \text{ceil}(r)\\ a_1 &= \text{floor}(a), \quad a_2 = \text{ceil}(a)\end{aligned} \tag{13}$$

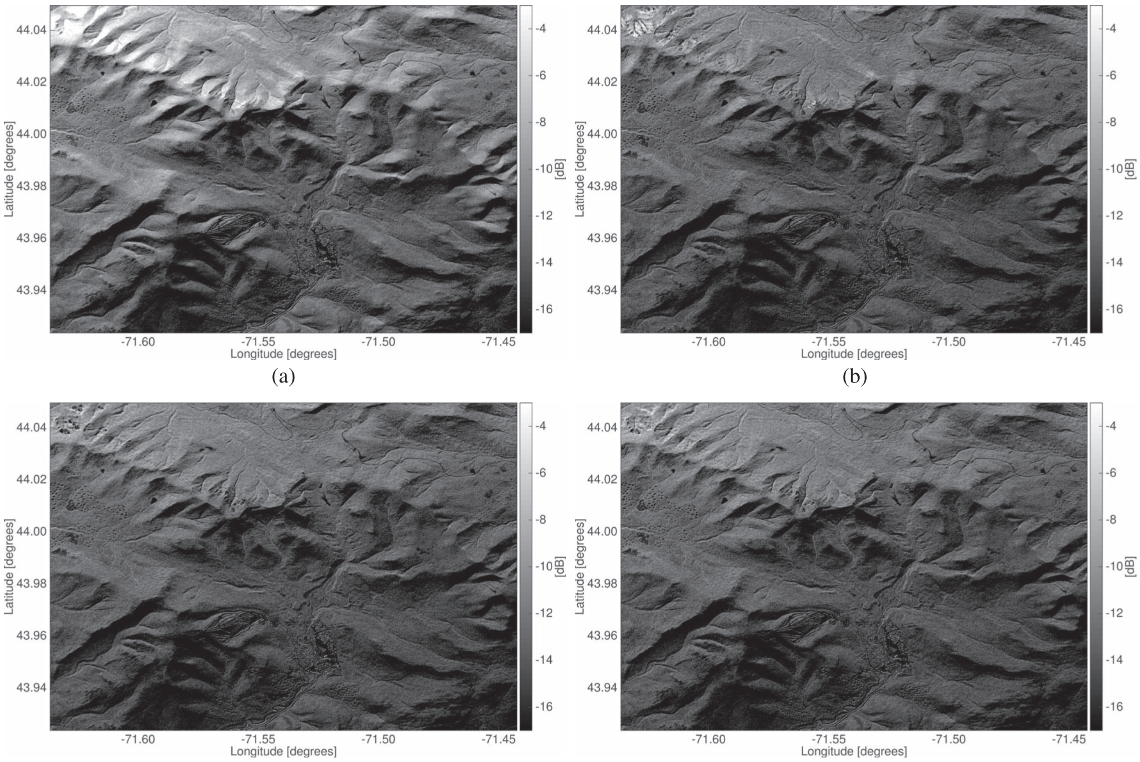

(a) (b) (c) (d)

Fig. 1. Radiometric calibration results, using the different area correction methods, for UAVSAR HV intensity images over White Mountain forests in New Hampshire. Calibration is most significant on slopes facing the radar (bright regions), although the $\sin\theta_i$ correction is often insufficient. (a) Uncorrected image. (b) Calibrated image using $\sin\theta_i$. (c) Calibrated image using $\cos\psi$. (d) Calibrated image using a heteromorphic/facet model.

where r and a are the fractional range and azimuth bins, respectively. The integer bounds are used as array indexes for the area image in radar coordinates. The bilinear distribution is performed as follows:

$$\begin{aligned}A_{a_2,r_2} &= A_{a_2,r_2} + (r - r_1)(a - a_1) * \text{area}\\ A_{a_2,r_1} &= A_{a_2,r_1} + (r_2 - r)(a - a_1) * \text{area}\\ A_{a_1,r_2} &= A_{a_1,r_2} + (r - r_1)(a_2 - a) * \text{area}\\ A_{a_1,r_1} &= A_{a_1,r_1} + (r_2 - r)(a_2 - a) * \text{area}\end{aligned} \tag{14}$$

where A is the area image in radar coordinates, and the quantity *area* is the area of the facet. The correction is performed in radar coordinates using (1). Often, the DEM spatial resolution is coarser than the SAR image producing blocky area estimates, which is the case here, since we used the 30-m Shuttle Radar Topography Mission (SRTM) elevation data set. We found that bilinear oversampling of the DEM, instead of nearest-neighbor approximation, resulted in a smoother and more realistic *area* image following integration (i.e., without blocky artifacts). Nominal oversampled spacing of ≈1/3 the DEM pixel spacing of the radar image was found to be sufficient.

C. Area Normalization Performance

Fig. 1 displays several HV intensity images in map geometry of a subset of the UAVSAR data acquired over the White Mountain National Forest in New Hampshire. Fig. 1(a) displays the uncorrected intensity image, whereas Fig. 1(b)–(d) shows radiometrically corrected images resulting from the different methods described in the previous section.

The brighter areas on slopes facing the radar are effectively corrected. Slopes facing away from the radar are also adjusted, although the topographic distortion in the images largely remains. This effect is due to changes in the interaction of the radar signal with the scatterers as a result of changing incidence angles and is an important factor when attempting to radiometrically correct vegetated terrain [3] and [5]. This issue will be discussed further in Section III. Fig. 2(a) displays the estimated illuminated area using the heteromorphic method in map geometry. The image serves as a simulation of the radar images, i.e., brighter areas in the radar image correspond to areas of higher illuminated area, and vice versa. Fig. 2(b) and (c) shows the differences in estimated area between the heteromorphic and the two homomorphic methods. Fig. 3 shows a map of the local incidence angle, for reference. While the calibrated radar images from the HPA and heteromorphic facet corrections are nearly identical, the local incidence angle displays significant difference in steeper facing slopes present in the near range, where the local incidence angle is below 25°.

Again, it is evident that the local incidence angle can both overestimate and underestimate the illuminated area depending on the geometry, particularly on higher slopes facing the radar. On those slopes, the homomorphic assumption is particularly prone to errors since several map pixels may be associated with the same radar pixel. The projection angle method combined with resampling to radar coordinates (i.e., HPA) agrees very well with the heteromorphic method and only has problems in the highest slopes facing the radar, where overestimation of the area occurs. This shows that the proposed resampling of area A

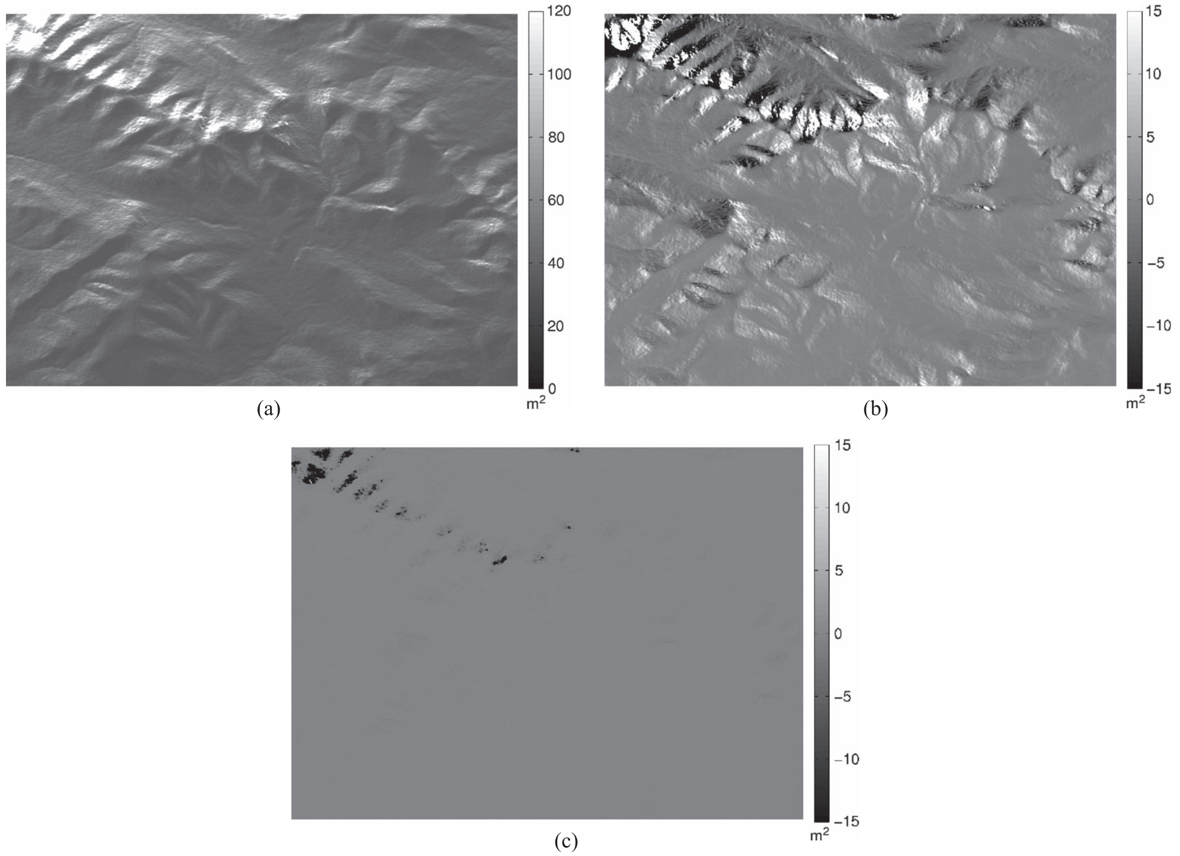

(a) (b)

(c)

Fig. 2. Estimated illuminated area and differences in estimated area between the different methods. There are significant differences between the facet and $\sin\theta_i$ predicted areas while HPA displays much closer results. (a) Estimated illuminated area using a facet model. (b) Area difference between the facet model and the $\sin\theta_i$ model. (c) Area difference between the facet model and the HPA ψ model.

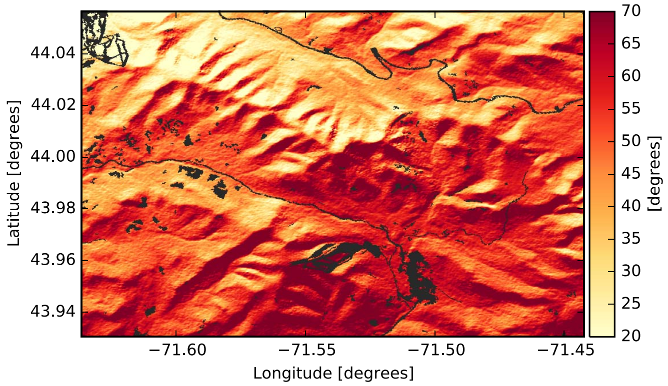

Fig. 3. Local incidence angle map, in degrees, with nonforested areas (urban, roads, etc.) shown in black. Values above 70° (dark red) are excluded from the analysis.

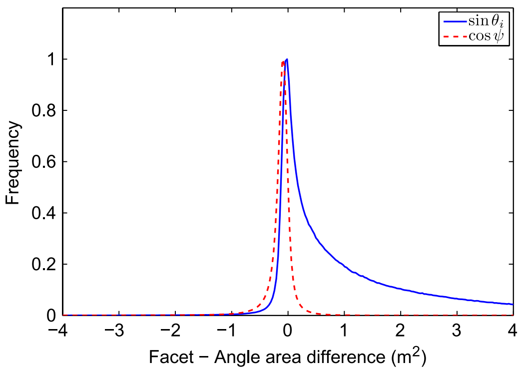

Fig. 4. Histogram of differences in area estimates between heteromorphic (facet) and angular methods. The wide peak in the $\sin\theta_i$ histogram indicates a large distribution of errors, whereas the sharp prominent peak in the $\cos\psi$ histogram shows close agreement with the heteromorphic method.

from map to radar coordinates partially mitigated the issue of information lost generally observed under the homomorphic assumption (i.e., one-to-one correspondence between a map and slant pixel). Fig. 4 displays a histogram of the area differences.

The local incidence angle method displays a bias toward underestimation of the area, with a widespread distribution of area errors. On the other hand, the HPA approach displays a very prominent and narrow peak near zero, which matches the results shown in Fig. 2. The area differences can be propagated to a radiometric calibration difference, where it was found that the HPA approach was within 0.5 dB of the facet model for most slopes.

Overall, the calibration results matched previous work comparing the homomorphic and heteromorphic methods [6]. The most problematic areas for homomorphic methods are steep slopes facing the radar, where the estimated illuminated area can be overestimated or underestimated. For these areas, a heteromorphic approach through DEM integration is more appropriate. The projection angle method coupled with resampling of the area to radar coordinates (i.e., HPA) provides a significant improvement to the local incidence angle model and shows a much closer agreement with the heteromorphic results.

The UAVSAR sensor is electronically steered in azimuth (α) to partially compensate for aircraft attitude. Nonzero steering angles result in modifications to the projection area by introducing additional components to the sensor-to-ground look vector (11). For example, it was found that for a steering angle of 8°, there was a residual $6\ \mathrm{m}^2$ of illuminated area for the near range on flat terrain, which can lead to calibration errors on the order of 0.5 dB. These geometries are not accounted for by the basic methods that integrate the DEM-derived facets as they assume broadside viewing. The broadside assumption is generally true for spaceborne systems but not for airborne systems, the orientation of which is strongly impacted by winds. The HPA model explicitly accounts for steering, yaw, pitch, and roll angles in the look vector (11) and, thus, provide appropriate geometry when used in our hybrid method.

The quality of any radiometric terrain correction is heavily dependent on the resolution of the DEM with respect to the radar backscatter image. However, with a DEM sampled at $\leq 1/3$ the pixel spacing of the radar image, the amount of computations required by heteromorphic methods is significantly increased.

The process of resampling the area image estimated from the projection angle often involves some form of averaging, which tends to cause a loss in resolution of the resultant area image in radar coordinates. Fine-scale features imaged by the radar may therefore be overcorrected or undercorrected depending on the viewing geometry and the resampling procedure chosen. This effect was observed in the slight overestimation of area by the HPA method coupled with an inverse distance weighted average.

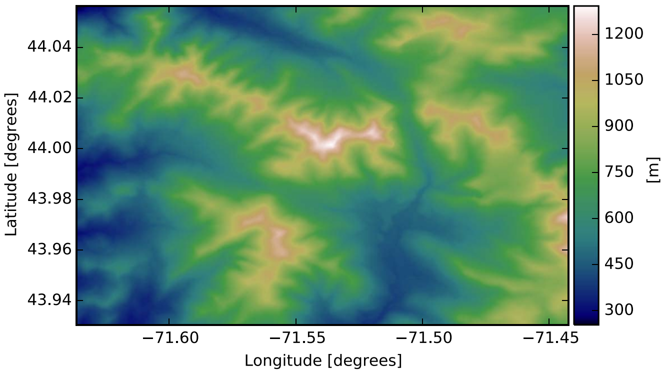

Fig. 5. Map of SRTM elevation, in meters, over the region of interest.

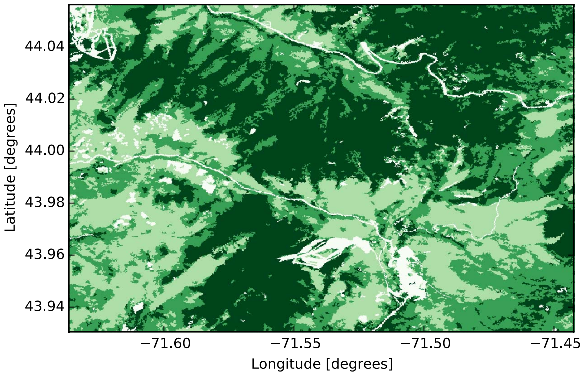

Fig. 6. Map of NLCD forest coverage over the region of interest. The three forest classes (41, 42, 43) are shown in different shades of green. From light to dark: deciduous forest (class 41), mixed forest (class 43), and evergreen (class 42). All other classes are shown in white.

III. RADIOMETRIC CORRECTION OF A FORESTED LANDSCAPE

In previous sections, we only considered the impact of illuminated area on the radar backscatter. However, the variation of forest reflectivity with viewing and terrain geometry remained, dominating the observed image features. Here, we introduce a new correction method specific to the radar imaging of forested landscapes with topography such that observed radiometry can be used to derive scientific products such as forest biomass irrespective of viewing geometry and topography. The proposed methodology considers the impact of viewing and target geometries independently through the use of the look angle and range slope. We demonstrate the method using UAVSAR data collected over the White Mountain National Forest of New Hampshire during the summer of 2009. To validate the performance of the radiometric correction, we used a pair of UAVSAR images collected from opposite aircraft headings. The two UAVSAR data sets used were the fully polarimetric multilook slant range complex images "Brtlet25101_09054_000_090805_L090_CX_01" and "Brtlet_07101_09054_001_090805_L090_CX_01," which will be referred to here as lines 1 and 2, respectively. Both data sets are available at http://uavsar.jpl.nasa.gov. Radiometric correction was performed in slant range geometry, and the results were then geocoded into geographic coordinates with 0.00005556° (5 m) pixel spacing. Within the images, we chose a rectangular subset of interest, covered by both flight lines and exhibiting significant topography. The subset was bounded by the coordinates 44.05632° N, 71.63655° W on the top-left corner and 43.93048° N, 71.44241° W on the bottom-right corner.

To perform the correction, we used the SRTM V2 DEM with 1 arc second (30 m) spacing. A map of the DEM over the subset of interest is shown in Fig. 5. The heights, referenced to the WGS84 ellipsoid, range from approximately 250 to 1300 m. Since we assess the calibration results using two flight lines with opposite aircraft headings, when reporting the results of the various corrections, we only include pixels visible to both lines. For these pixels, the range slopes vary from -31° to 30°.

We selected forested areas using the 2011 National Land Cover Dataset (NLCD) [13] produced from Landsat data. A map of NLCD forest coverage for the region of interest is shown in Fig. 6. The NLCD has a spatial resolution of 30 m, and a pixel may encompass several ground areas that are captured by the 5-m UAVSAR data within an NLCD pixel. To characterize the backscatter of forest pixels only, we selected radar pixels with HV backscatter intensity greater than 0.02 (i.e., -17 dB). In the density plots and histograms later in this paper, we only include data for these pixels that are both forested according to the NLCD and have HV $\sigma^0 > -17$ dB. We also exclude all pixels

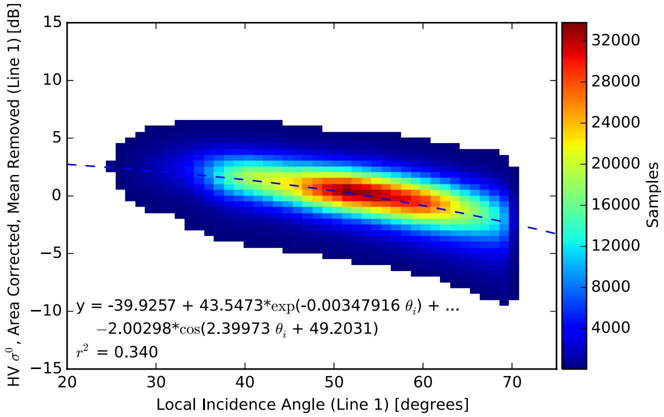

Fig. 7. HV σ^0 (dB) of line 1, after area correction and shifted to have zero mean, versus the local incidence angle. The blue line is the fitted normalization function for the cosine correction, with equation and r^2 as shown on the plot.

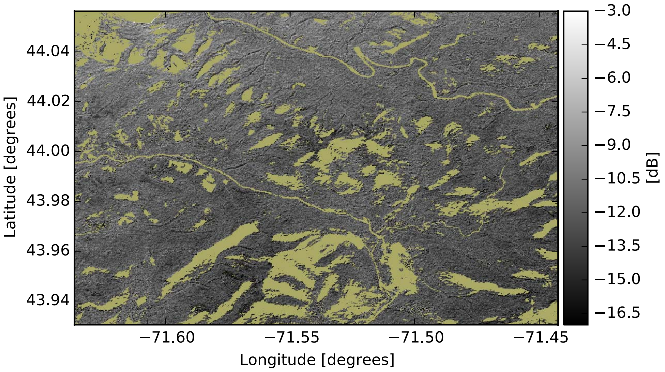

Fig. 8. HV σ^0 (dB) image for line 1, using the $1/\cos{\theta_i}^n$ correction. The yellow areas are nonforested or have a local incidence angle greater than 70°.

located in areas behind the steep topographic feature using a threshold set to a maximum local incidence angle of 70°.

A. Cosine Function Correction

We compare the new method presented in Section III-C to the cosine function, which is often used to correct for terrain topography through the use of a variety of different empirical models based on various functions of $\cos\theta_i$ [14], [15]. Radar backscatter over forest surfaces has been shown to be best fitted by functions of $1/\cos(\theta_i)^n$, where the parameters are a function of land cover type, polarization, and frequency, over the limited range of incidence angles provided by spaceborne sensors [5], [16].

Fig. 7 shows the measured HV backscatter, for line 1, plotted against local incidence angle. The data are plotted in decibels, with the mean removed, to compare its shape against the fitted function. The fitted correction function, also in decibels, has equation $y = -39.9257 + 43.5473\exp(-0.00347916\theta_i) - 2.00298\cos(2.39973\theta_i + 49.2031)$, and $r^2 = 0.34$, for θ_i in degrees. The radar images (both 1 and 2) are then normalized by the function fit (i.e., shifted by the function fit in decibels) in radar geometry to finally obtain the radiometrically calibrated HV intensity image such as that shown in Fig. 8 (showing image for line 1).

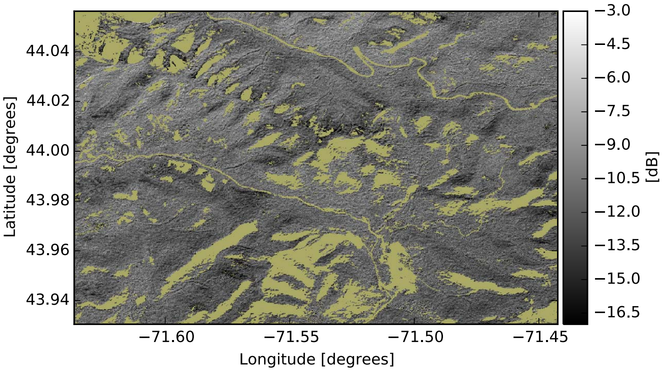

Fig. 9. HV γ^0 (dB) image, using the first-stage N_1 correction from [5]. The yellow areas are nonforested or have a local incidence angle greater than 70°.

B. Two-Stage Correction Model

Recently, a two-stage semiempirical model was proposed in [5], validated using spaceborne ALOS PALSAR data, yielding residual radiometric correction errors of less than 1 dB over the test areas. Stage one of the model was based on the use of one of two potential correction factors, of which the first yielded the best results and will be the one discussed here [5]. This correction factor, referred to as N_1, treats the terrain as an opaque volume of isotropic scatterers and can be defined by the following equation [5]:

$$\gamma^0 = \gamma_f^0 \frac{\tan(90^\circ - \theta_l + \tau_\rho)}{\tan(90^\circ - \theta_l)} = \gamma_f^0 N_1(\theta_l, \tau_\rho) \tag{15}$$

where γ^0 is the backscatter from the tilted terrain, equivalent to σ^0 divided by the cosine of the local incidence angle for flat terrain; γ_f^0 is the backscatter from flat terrain; θ_l is the look angle (i.e., the local incidence angle for flat terrain); and τ_ρ is the slope angle in the range direction [5]. Note that this model uses γ^0 rather than σ^0. For consistency with [5], we have also used γ^0 when referring to this model and when reporting its results in this paper. However, the other corrections tested in later sections use the σ^0, as in (1).

After applying the first-stage correction, the resulting data were used to fit the second stage of the model, the correction factor M_1, which is defined by the residual local incidence angle and azimuth slope dependence through a function of the following form [5]:

$$M_1 = \frac{f_\Delta(\theta_i) \cdot f_{\mathrm{az}}(\tau_s)}{f_\Delta(\theta_l)} \tag{16}$$

where f_Δ is a marginal function modeling the residual local incidence angle dependence of the data, f_{az} is a marginal function modeling the residual azimuth slope dependence of the data, θ_i is the local incidence angle, and τ_s is the slope angle in the azimuth direction [5]. Once M_1 is fitted, the final corrected γ_f^0 can be calculated from the equation $\gamma^0 = \gamma_f^0 N_1 M_1$ [5].

Both marginal functions used to form M_1 are functions of $\cos^n$, where $f_\Delta = \cos^a(\theta) + c \cdot \cos^b(\theta)$, and $f_{\mathrm{az}} = \cos^d(\tau_s)$ [5]. f_Δ is fitted using the local incidence angle and is evaluated using that incidence angle in the numerator of M_1, but is

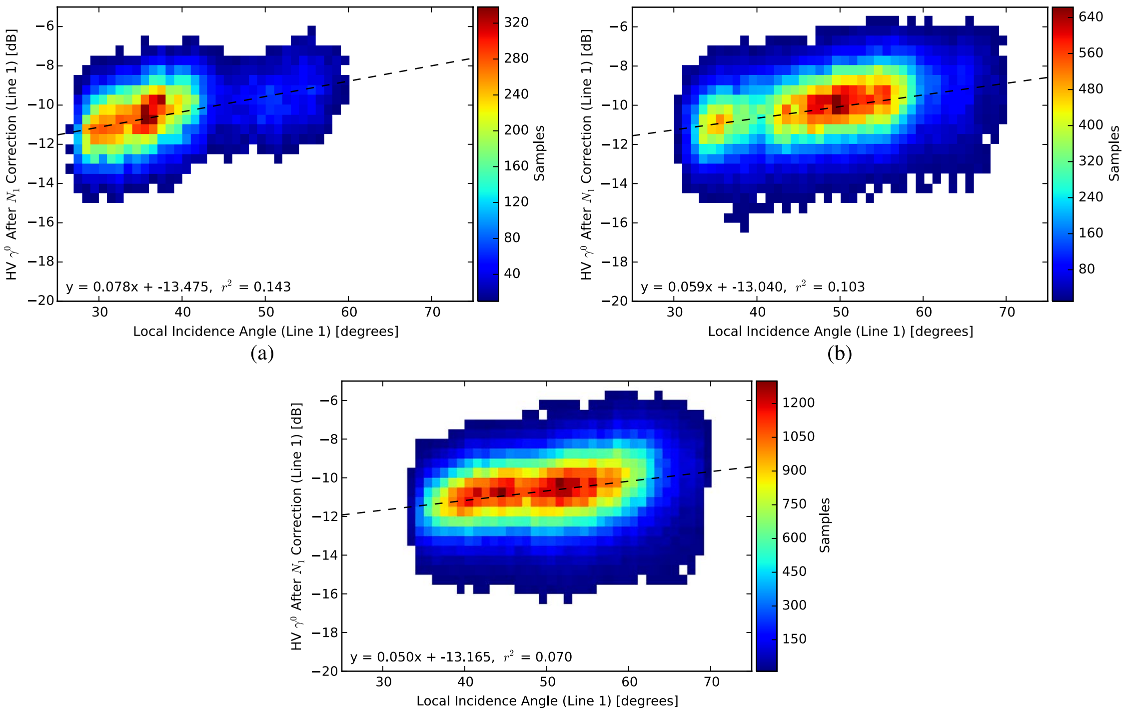

(a) (b) (c)

Fig. 10. Density plots of HV γ^0 (dB) values after N_1 correction as in [5], for each look angle range, versus local incidence angle (degrees). The black lines are best fit lines with equation and r^2 as shown on each plot. (a) 34°–35° look angle. (b) 39°–40° look angle. (c) 44°–45° look angle.

evaluated using the look angle θ_l in the denominator (i.e., as if there were no slope effects) [5]. It was found that the use of the second stage of the model was mostly only necessary in areas with sparse vegetation cover such as woodland, where the assumption of isotropic backscatter is not necessarily valid [5]. In dense forests with few open areas, often, the first stage of the model was sufficient to remove most of the topographic effects, and therefore, M_1 was set to unity [5]. In this sense, the two-stage model can be looked at as an extension of other empirical models based on cosine functions in the literature (e.g., the models in [15]), with the added step that the two-stage model attempts to account for different types of land cover within a single scene, applying the second stage [i.e., (16)] only when necessary [5]. We corrected the line-1 HV intensity using the N_1 correction factor as in (15), resulting in the corrected image shown in Fig. 9.

Since our study area is made up of closed forest almost exclusively, it is tempting to assume that M_1 is equal to unity for our data set, as it was for closed forest in [5]. To prove or disprove this assumption, we attempted to measure the residual dependence on local incidence angle after performing the N_1 correction. To fit M_1 to the data, the work in [5] chose data within a small look angle range (of about one degree), but across a wide variety of range and azimuth slopes, resulting in as much variation in local incidence angle as possible. Therefore, they modeled the backscatter variation as a function of target geometry, with the viewing geometry mostly fixed. Similarly, we plotted the HV γ^0 values from the first-stage correction, for three look angle ranges, versus the local incidence angle of each pixel, as shown in Fig. 10. It is clear that while there is residual dependence on the local incidence angle in the N_1 corrected image, this dependence is also unfortunately a function of the look angle. For the 34°–35° look angles, the best fit line has a slope of 0.078 dB/degree, whereas for the 44°–45° look angles, the best fit line has a slope of only 0.050 dB/degree. As the look angle increases, the residual local incidence angle dependence is decreased. Therefore, the model parameters of $f_\triangle$ are themselves a function of look angle for our study area. Since the two-stage correction model in [5] was applied to spaceborne data, where the look angle range across the swath was only about 4°, this was not an issue in that case. However, for the wide range of viewing geometries contained in airborne data, we would need to fit different $f_\triangle$ across the swath. While this is certainly possible, it would also be time consuming, and so, we have taken a different approach wherein we attempt to empirically model the residual topographic effects as a 2-D function of look angle and range slope, as described in the next section.

C. Radiometric Correction Based on Viewing and Target Geometry

Instead of performing a correction based on the local incidence angle or a simple difference between the look angle and the range slope, we now consider the effects of the look angle θ_l and the range slope τ_ρ independently. Since an infinite number of combinations of θ_l and τ_ρ can lead to the same θ_i, splitting the contributions of the viewing and target geometries this way allows us to account for the fact that the backscattering mechanisms of vegetation change with look and slope in

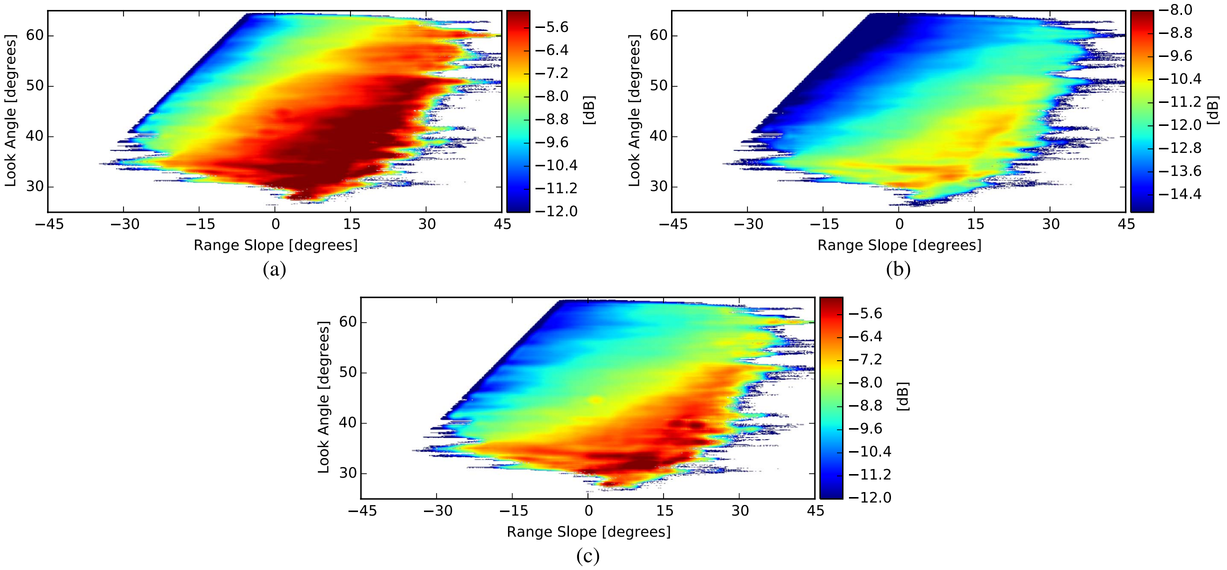

Fig. 11. Average backscatter values (in decibels) over vegetated areas of both lines, as a function of look angle θ_l and range slope τ_ρ. (a) HH lookup table. (b) HV lookup table. (c) VV lookup table.

different ways [2], [3], [5]. We computed the average backscatter intensity for each polarization as a 2-D function of θ_l (i.e., the viewing geometry) and τ_ρ. The latter characterizes the angle between the surface and the vertical tree (i.e., the target geometry) in the view plane. On flat terrain, trees stand around 90°, providing the highest ground-trunk scattering. As the terrain slope increases, the contribution of the ground-trunk scattering mechanism decreases. The greatest impact occurs in the HH and VV polarization channels, but the effect is still significant in the HV polarization.

Fig. 11 shows the lookup tables (LUTs) generated from the data, computed as the average over all forest pixels (within both lines) as a function of θ_l and τ_ρ with 0.1° bins in the slope and 0.2° bins in the look angle. Using a look angle range of 0°–90° and a slope range of −90° to 90°, this yielded a 900 × 900 element LUT. After calculating the mean value of each bin from the data, we then smoothed the LUTs using a Savitzky–Golay filter [17] with a window size of 21 × 21 and an order of 3. The Savitzky–Golay filter essentially smooths the data using a moving window by fitting a polynomial to the data points within the window and then using the fitted polynomial to calculate a new value for the center point [17]. Note that the available backscatter values are constrained within the look angle versus slope space. The diagonal edge at the left side of the available data represents the boundary where the combinations of look angle and slope begin to produce a negligible illuminated area (i.e., the look vector and the ground surface are almost parallel). The top and bottom edges represent the limits of the UAVSAR look angle in the subset. The LUT values are also restricted to the range of slope values available in the data, shown by the jagged edges at the bottom left and at the right. Note that the variation in backscatter values is more complicated than could be accounted for solely through the use of the local incidence angle.

Radiometric correction is performed by normalizing the radar image using these values. Each pixel's backscatter value is multiplied by the ratio between the LUT value for $\tau_\rho = 0°$ and $\theta_l = 35°$ (representing neutral geometry) and the LUT value corresponding to the given pixel's look angle and slope, as in the following equation:

$$\sigma^0_{\text{final}} = \sigma^0_{\text{area}} \frac{\text{LUT}_{0°,35°}}{\text{LUT}_{\tau_\rho,\theta_l}} \tag{17}$$

where σ^0_{area} is the calibrated σ^0 (in linear units) after area correction (using the HPA method described in Section II-A2), σ^0_{final} is the final σ^0 value (in linear units) after range slope and look angle correction, and LUT is the corresponding LUT value for the subscripted range slope and look angle.

Note that the dynamic range of the LUT values is 10–11 dB for the HH and VV polarizations, but only 6.7 dB for the HV polarization.

D. *Validation of Radiometric Correction*

Fig. 12 shows HV σ^0 images for lines 1 and 2, for both the uncorrected data and for data corrected using the LUT method. Fig. 12(a) and (b) shows the two uncorrected images, where the topographic effects are clearly visible. In line 1, the brightest areas of the image are in the top left, in the near range of the radar. In line 2, the brightest areas of the image are in the bottom right due to the opposite aircraft heading. Fig. 12(c) and (d) shows the two corrected images, where the radiometric calibration has removed most of the topographic features. However, high-resolution features such as mountain peaks and forest boundaries perpendicular to the look direction are still visible. This is mainly due to the SRTM DEM that does not have sufficient spatial resolution to resolve these features. On the other hand, forest boundaries form a wall with particularly strong ground-trunk scattering or shadow depending on the line of sight.

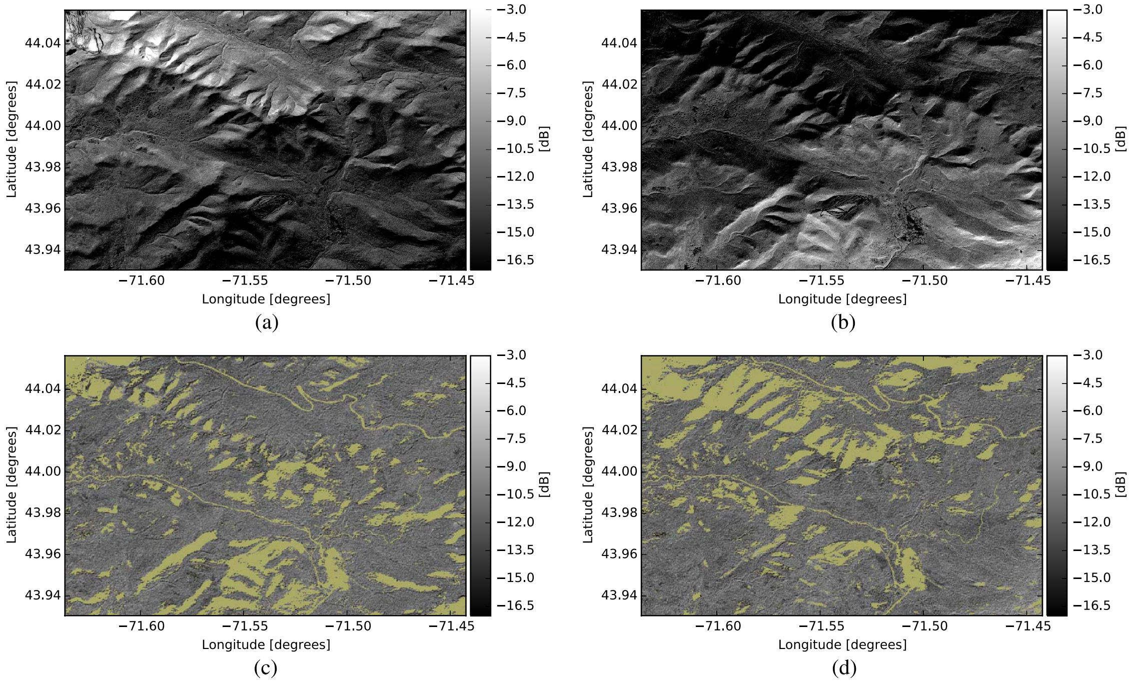

Fig. 12. HV σ^0 (dB) images, for line 1 (left column) and line 2 (right column), without radiometric correction (top row) and with LUT correction (bottom row). In the corrected images, the yellow areas are nonforested or have a local incidence angle greater than 70°. (a) Line 1—No Correction. (b) Line 2—No Correction. (c) Line 1—LUT Correction. (d) Line 2—LUT Correction.

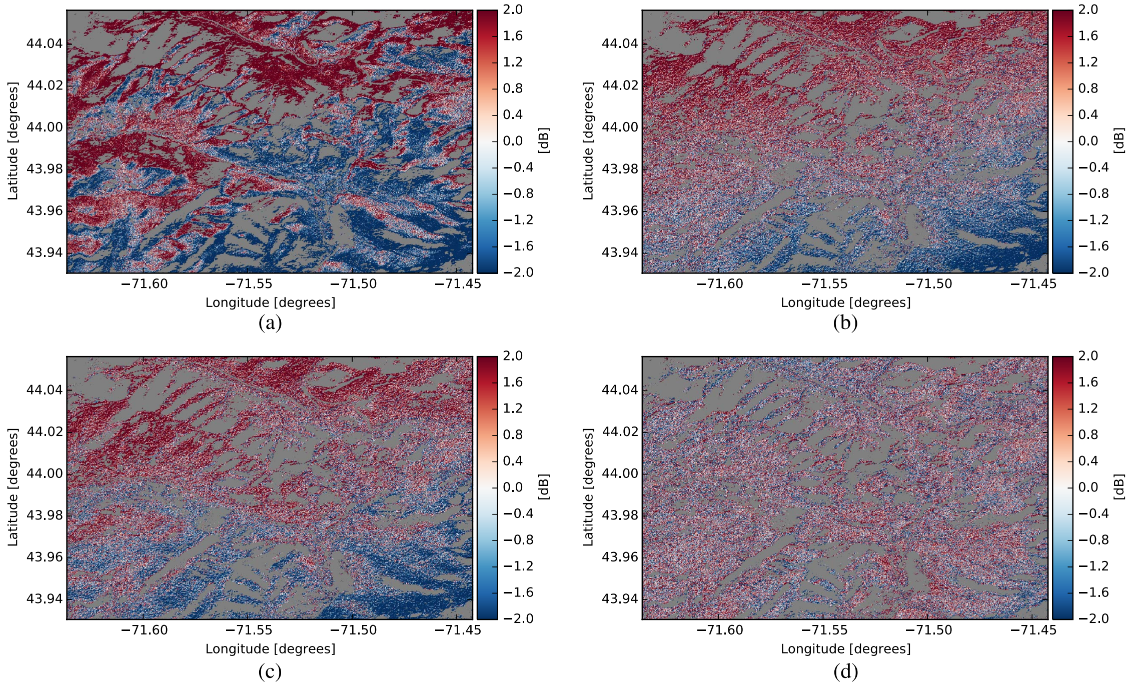

Fig. 13. HV ratio (in decibels) of lines 1 and 2. Gray areas represent masked areas where the radiometric calibration could not be performed (for either line). (a) No Radiometric correction. (b) Cosine correction. (c) N_1 Correction. (d) LUT correction.

For ecological applications such as biomass retrieval, pixels of a given forest patch should ideally exhibit the same backscatter intensity from the opposite view points, that is, even if the proportions of the scattering mechanisms change with geometry. This implies that the backscattering ratios are not preserved and will be forced to be constant throughout the radar swath.

Fig. 13 shows images of the HV backscatter ratio of line 1/line 2, for (a) the uncorrected images, (b) images corrected using the cosine method, (c) images corrected using the N_1 correction in [5], and (d) images corrected using our LUT method. For the N_1 correction, the ratio is the γ^0 ratio, to be consistent with [5], whereas for the other corrections, the ratio shown is the σ^0 ratio. For well-corrected images, we would

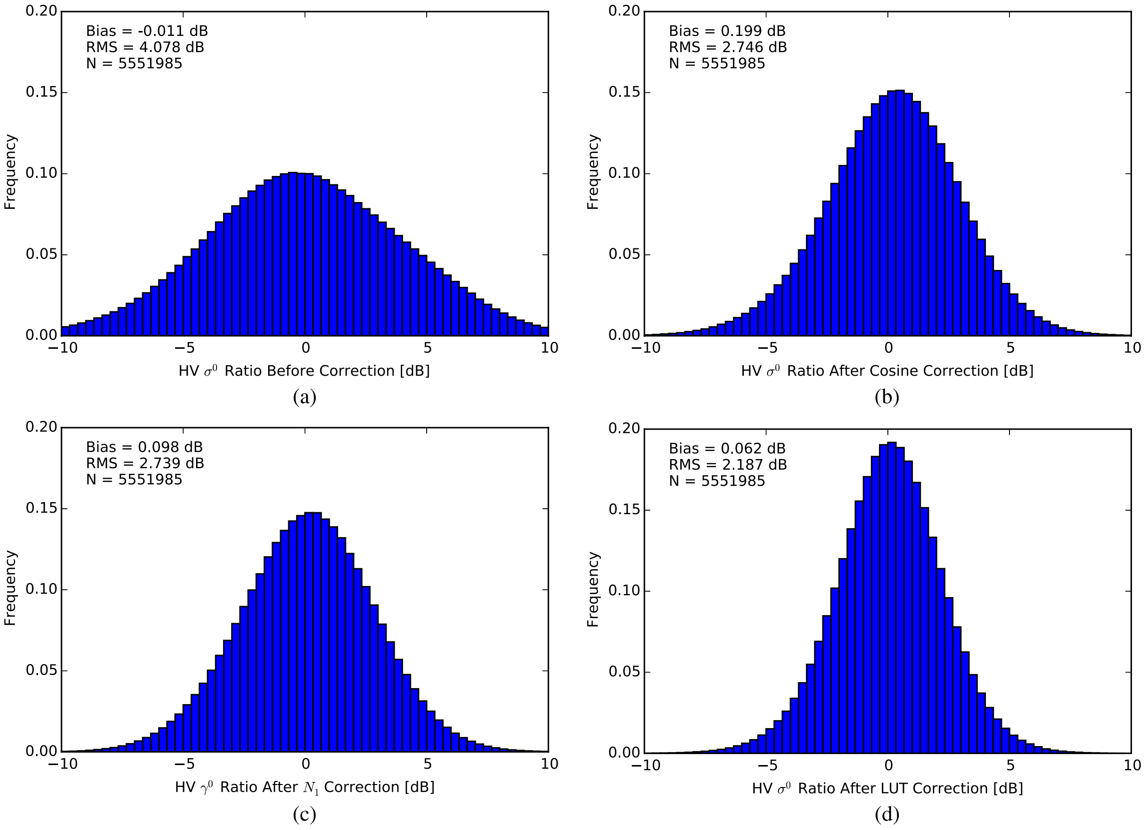

(a) (b) (c) (d)

Fig. 14. Histograms of the HV ratio values (in decibels) of lines 1 and 2. (a) No Radiometric correction. (b) Cosine correction. (c) N_1 Correction. (d) LUT correction.

like the HV ratio values to be close to 1 and to exhibit little, if any, dependence on geometry. In the uncorrected, $1/\cos^n$ corrected, and N_1 corrected images, a strong gradient is visible, with mostly positive HV ratios in the top left and negative HV ratios in the bottom right, aligned with the look direction of the radar and, therefore, presumably indicative of residual geometric effects that are a function of local incidence angle. This gradient is less apparent in the LUT corrected image, and the overall errors in this image are also smaller.

Fig. 14 shows histograms of the HV σ^0 ratio values, for each of the three corrections. Areas with local incidence angle $> 70^\circ$ (as seen by either line) are excluded from the histograms and from all subsequent plots and statistics, so that only radiometrically corrected pixels are considered. All of the corrections show a large improvement as compared with the uncorrected data. The root mean square (RMS) values of the cosine and N_1 corrections are fairly similar, although the cosine correction introduced a 0.20-dB bias that was not present in the original data (whereas the bias of the N_1 correction is only 0.1 dB). Moreover, worth noting is that while the cosine correction and the N_1 correction yielded similar RMS values, the cosine correction was fitted to the data, whereas the N_1 correction is based purely on geometry, with no fitted parameters necessary. The LUT correction produces the smallest RMS ratio value, as well as the smallest bias of the three corrections. It is important to note that the LUT is fitted to the current vegetation type, and new LUTs should be developed for other vegetation types or study areas.

For well-corrected images, in addition to the HV ratio being small, the ratio values would not exhibit any residual dependence on range slope or look angle. We therefore wish to measure whether the ratio values are correlated to the geometry. Fig. 15 shows density plots (2-D histograms) of the HV ratio between the two images as a function of the range slope seen by line 1. Similarly, Fig. 16 shows density plots of the HV ratio as a function of the line-1 look angle. Ideally, the best fit line for the corrected images would have the equation $y = 0$. We found a residual dependence on range slope and look angle exhibited by all three corections. However, the residual was significantly smaller in the LUT correction with the HV σ^0 ratio's dependence on range slope and look angle being 0.003 dB/degree for both angles. These are more than an order of magnitude smaller than the other corrections.

Furthermore, of note is the fact that the uncorrected data, as one might expect, display a positive correlation with range slope. That is, as the line-1 range slope increases, we would expect the line-1 backscatter to increase. Since a positive range slope as seen in line 1 is a negative range slope as seen in line 2, we would therefore expect the HV ratio to increase monotonically with line-1 range slope (and to decrease monotonically with line-2 range slope). However, for both the cosine and N_1 corrections, the opposite is the case. This implies that these corrections are actually slightly overcorrecting for the range slope effects. In contrast, these two corrections undercorrect for the look angle effects.

Finally, we have not yet considered the effects of the azimuth slope. Fig. 17 shows density plots of the HV ratio versus the absolute value of the line-1 azimuth slope for each correction. The dependence of the uncorrected HV ratio on the azimuth slope is

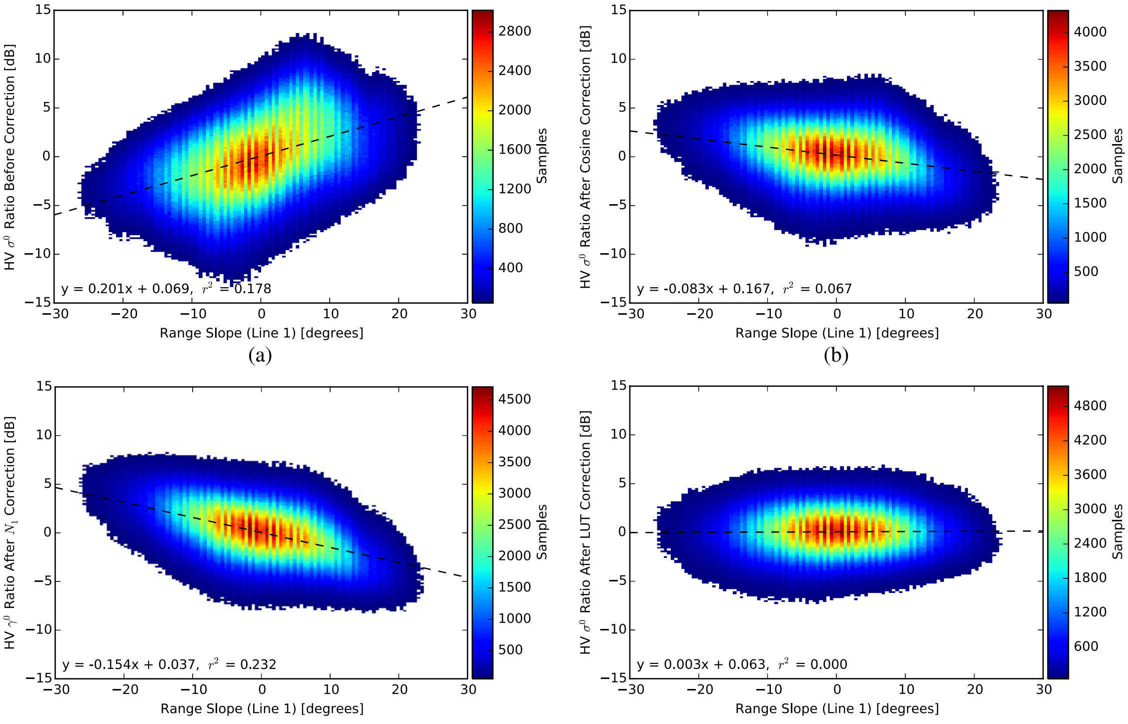

(a) (b) (c) (d)

Fig. 15. Density plots of the HV ratio values (in decibels) versus the range slope as seen by line 1. The blue lines are best fit lines with equation and r^2 as shown on each plot. (a) No Radiometric correction. (b) Cosine correction. (c) N_1 correction. (d) LUT correction.

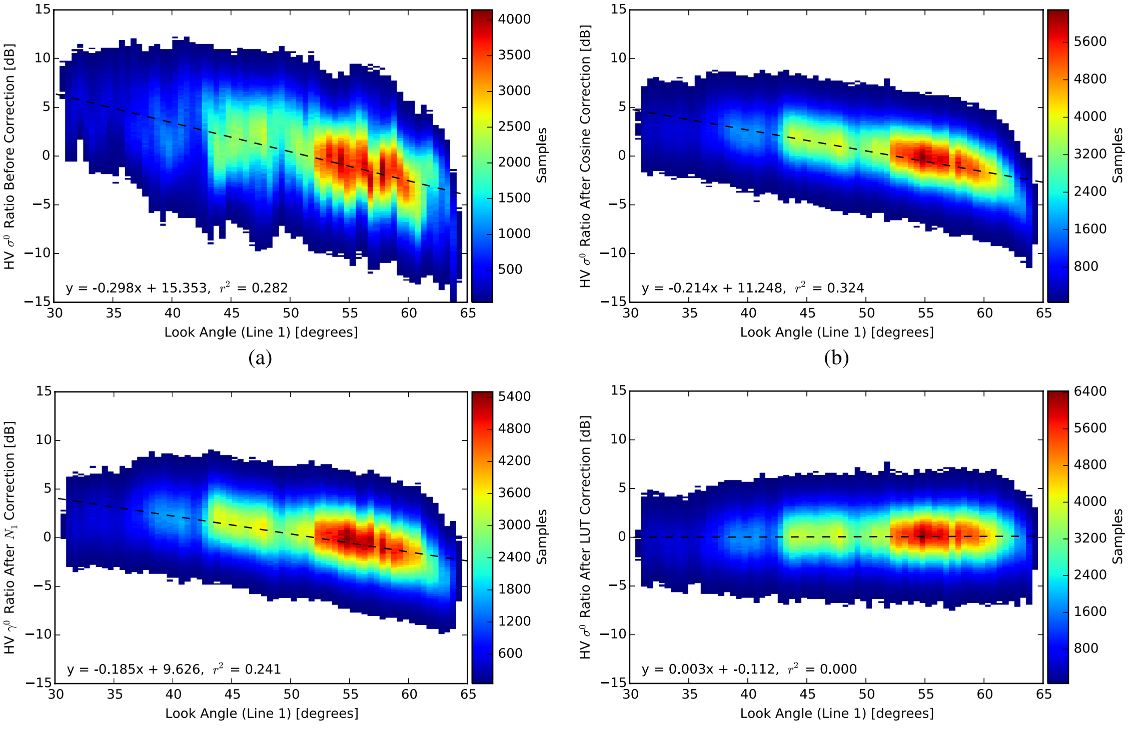

(a) (b) (c) (d)

Fig. 16. Density plots of the HV ratio values (in decibels) versus the look angle of line 1. The blue lines are best fit lines with equation and r^2 as shown on each plot. (a) No Radiometric correction. (b) Cosine correction. (c) N_1 correction. (d) LUT correction.

already quite small, at only 0.002 dB/degree. The residual dependence relations on azimuth slope in the corrected images are actually larger than those in the uncorrected image, but are all still quite small. For the LUT correction, it is −0.006 dB/degree.

IV. CONCLUSION

We began by reviewing a number of different radiometric calibration techniques common in the literature, all based on various methods to calculate the area illuminated by the SAR

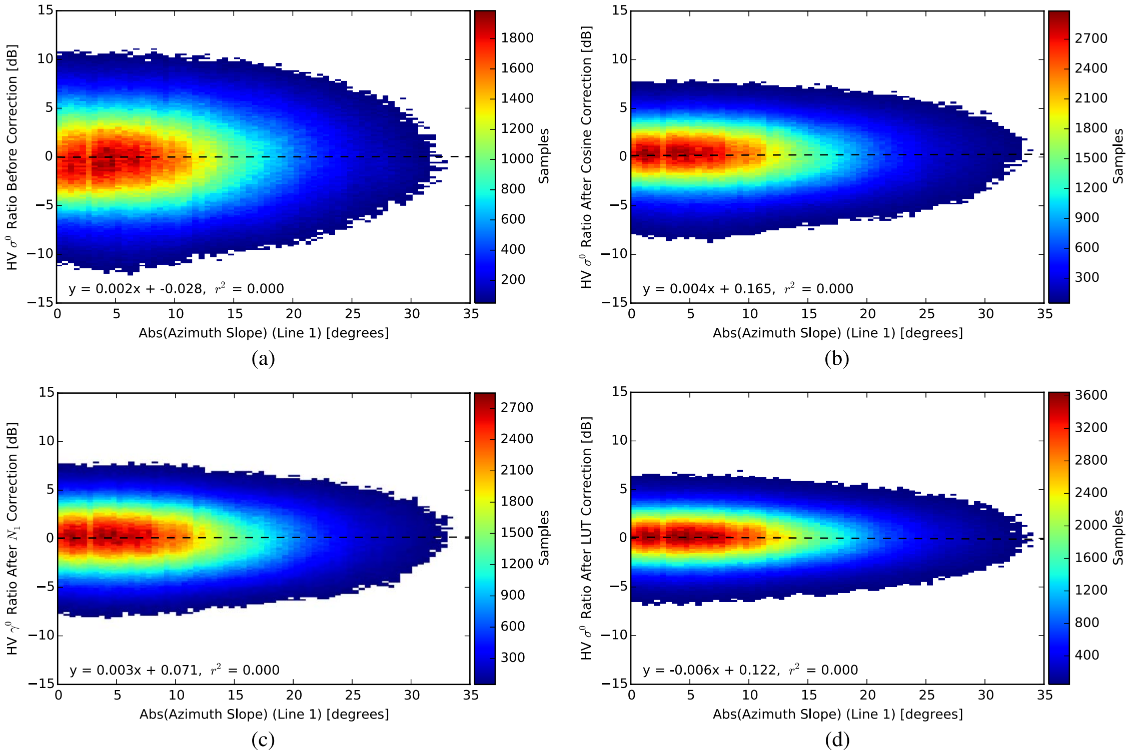

(a) (b) (c) (d)

Fig. 17. Density plots of the HV σ^0 ratio values (in decibels) versus the azimuth slope seen by line 1. The blue lines are best fit lines with equation and r^2 as shown on each plot. (a) No Radiometric correction. (b) Cosine correction. (c) N_1 correction. (d) LUT correction.

sensor. We demonstrated that a combination of the heteromorphic and homomorphic methods, called the HPA method, yields better results than homomorphic calibration using the local incidence angle (improvement of up to 5dB), while still being generally faster to compute than full heteromorphic correction using DEM integration. We then demonstrated a new method for radiometric calibration over vegetated terrain with significant topographic features. This method is performed after area correction using the HPA method and is based on the calculation of average backscatter values for vegetation as a 2-D function of the look angle and the range slope. These values are stored in an LUT, and the measured backscatter values for each pixel are then normalized using the appropriate LUT value corresponding to their look angle and range slope. This way, we are able to account for the effects of the viewing geometry and target geometry independently during the radiometric correction process, allowing more accurate calibration than is possible using the local incidence or projection angle alone.

Our study area contained predominantly closed canopy forests, of deciduous, coniferous, and mixed type. We were able to use a single LUT to account for all of the vegetated land cover in our study area. When working in a more diverse study area, the use of different LUTs for each land cover type may be necessary. Our method therefore relies on the fact that this land cover information is available. In this paper, we used the National Land Cover Database [13], but potentially, other types of ancillary data could be used.

We demonstrated the results of our calibration using UAVSAR data of the White Mountain area of New Hampshire. The same area was imaged from two opposite flight headings, and we validated our approach by taking the HV σ^0 ratio between the two corrected images. For well-corrected images, we would expect the HV ratio to be small and independent of the slope and look angle. We compared the new method to a correction using the function $1/\cos{\theta_i}^n$, as well as to the first stage of the two-stage model in [5]. The new LUT correction method yielded better HV ratio values than that of the other corrections, with an RMS value of 2.19 dB (compared with 2.75 dB for the cosine correction and 4.08 dB for the uncorrected images).

As well, the HV σ^0 ratio from the LUT correction, when plotted against slope and look angle, exhibited less residual dependence on geometry than the other two corrections. The residual dependence relations on range slope and look angle were 0.003 dB/degree for both parameters. Much of the previous work in the literature regarding radiometric correction of SAR images has focused on spaceborne data with a limited range of look angles, where the viewing geometry therefore plays a smaller role in the observed topographic effects than the target geometry. When working with data that have a wide range of look angles (such as airborne data and potentially spaceborne ScanSAR data), such as the UAVSAR data used in this study, both the viewing and target geometries must be carefully considered and accounted for. The proposed HPA-LUT correction could be applied to spaceborne and nonsteerable radar systems by setting appropriate parameters to zero in (11).

Acknowledgment

The authors would like to thank the anonymous peer-reviewers for the contributions.

REFERENCES

[1] D. J. Goering, H. Chen, L. D. Hinzman, and D. L. Kane, "Removal of terrain effects from SAR satellite imagery of arctic tundra," *IEEE Trans. Geosci. Remote Sens.*, vol. 33, no. 1, pp. 185–194, Jan. 1995.

[2] A. J. Luckman, "The effects of topography on mechanisms of radar backscatter from coniferous forest and upland pasture," *IEEE Trans. Geosci. Remote Sens.*, vol. 36, no. 5, pp. 1830–1834, Sep. 1998.

[3] G. Sun, K. J. Ranson, and V. I. Kharuk, "Radiometric slope correction for forest biomass estimation from SAR data in the Western Sayani Mountains, Siberia," *Remote Sens. Environ.*, vol. 79, no. 2/3, pp. 279–287, Feb. 2002.

[4] D. K. Atwood, D. Small, and R. Gens, "Improving PolSAR land cover classification with radiometric correction of the coherency matrix," *IEEE J. Sel. Topics Appl. Earth Observ. Remote Sens.*, vol. 5, no. 3, pp. 848–856, Jun. 2012.

[5] D. H. Hoekman and J. Reiche, "Multi-model radiometric slope correction of SAR images of complex terrain using a two-stage semi-empirical approach," *Remote Sens. Environ.*, vol. 156, pp. 1–10, Jan. 2015. [Online]. Available: http://linkinghub.elsevier.com/retrieve/pii/S0034425714003575.

[6] D. Small, "Flattening gamma: Radiometric terrain correction for SAR imagery," *IEEE Trans. Geosci. Remote Sens.*, vol. 49, no. 8, pp. 3081–3093, Aug. 2011.

[7] L. M. H. Ulander, "Radiometric slope correction of synthetic-aperture radar images," *IEEE Trans. Geosci. Remote Sens.*, vol. 34, no. 5, pp. 1115–1122, Sep. 1996.

[8] D. Small, F. Holecz, E. Meier, and D. Nüesch, "Absolute radiometric correction in rugged terrain: A plea for integrated radar brightness," in *Proc. IGARSS*, 1998, pp. 6–10.

[9] Q. Zhou and X. Liu, "Error analyais on grid-based slope and aspect algorithms," *Photogramm. Eng. Remote Sens.*, vol. 70, no. 8, pp. 957–962, Aug. 2004.

[10] G. Leclerc, N. Beaulieu, and F. Bonn, "A simple method to account for topography in the radiometric correction of radar imagery," *Int. J. Remote Sens.*, vol. 22, no. 17, pp. 3553–3570, 2001.

[11] S. Hensley *et al.*, "Residual motion estimation for UAVSAR: Implications of an electronically scanned array," in *Proc. IEEE Radar Conf.*, 2009, pp. 1–5.

[12] A. Beaudoin *et al.*, "On the use of ERS-1 SAR data over hilly terrain: Necessity of radiometric corrections for thematic applications," in *Proc. IEEE IGARSS*, Jul. 1995, pp. 2179–2182.

[13] S. Jin *et al.*, "A comprehensive change detection method for updating the National Land Cover Database to circa 2011," *Remote Sens. Environ.*, vol. 132, pp. 159–175, May 2013.

[14] M. Hinse, Q. H. J. Gwyn, and F. Bonn, "Radiometric correction of C-band imagery for topographic effects in regions of moderate relief," *IEEE Trans. Geosci. Remote Sens.*, vol. 26, no. 2, pp. 122–132, Mar. 1988.

[15] T. Bayer, R. Winter, and G. Schreier, "Terrain influences in SAR backscatter and attempts to their correction," *IEEE Trans. Geosci. Remote Sens.*, vol. 29, no. 3, pp. 451–462, May 1991.

[16] T. Castel *et al.*, "Sensitivity of space-borne SAR data to forest parameters over sloping terrain. Theory and experiment," *Int. J. Remote Sens.*, vol. 22, no. 12, pp. 2351–2376, 2001.

[17] A. Savitzky and M. J. E. Golay, "Smoothing and differentiation of data by simplified least squares procedures," *Anal. Chem.*, vol. 36, no. 8, pp. 1627–1639, Jul. 1964. [Online]. Available: http://dx.doi.org/10.1021/ac60214a047

Marc Simard received the Ph.D. degree from the Université Laval, Quebec City, QC, Canada, in 1998.

He is a Senior Scientist with the Radar Science and Engineering Section, Jet Propulsion Laboratory (JPL), National Aeronautics and Space Administration, Pasadena, CA, USA. Since then, he has been with JPL, working on several science projects and flight missions (AIRSAR, GeoSAR, UAVSAR, WSOA, SWOT, and NISAR). His expertise is in algorithm development of products for ecological scienceapplications based on active remote sensing. He is particularly interested in the fusion of large- and small-footprint lidars, synthetic aperture radar (SAR), and interferometric SAR to produce 3-D renditions of volumes and surfaces such as vegetation canopy and topography over large geographical areas.

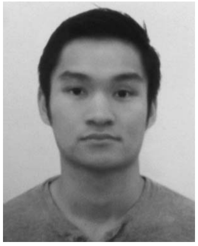

Bryan V. Riel received the B.Sc. degree and the M.Sc. degree in geophysics from the California Institute of Technology, Pasadena, CA, USA, where he is currently working toward the Ph.D. degree in geophysics. His graduate research was focused on the radiometric calibration of synthetic aperture radar (SAR) data and quantification of elevation errors in backscatter products.

His current research interests include geodetic observations of surface deformation, inverse theory, and time-series analysis of Global Positioning System and interferometric SAR data.

Mr. Riel received the National Aeronautics and Space Administration Earth and Space Sciences Fellowship in 2012.

Michael Denbina received the B.Sc. degree in electrical engineering and the Ph.D. degree in geomatics engineering from the University of Calgary, Calgary, AB, Canada, in 2010 and 2015, respectively. His Ph.D. research was on the use of compact polarimetric synthetic aperture radar (SAR) for the detection and discrimination of icebergs.

In 2015, he became a Postdoctoral Program Fellow with the National Aeronautics and Space Administration Jet Propulsion Laboratory, Pasadena, CA, USA, where he is working on methods for the mapping of vegetation height and structure using polarimetric synthetic aperture radar (SAR) interferometry. His research interests include the use of SAR for the retrieval of many types of environmental parameters and the investigation of algorithms for that purpose.

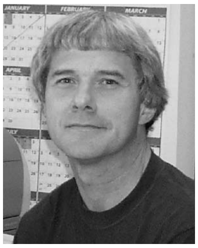

Scott Hensley received the B.S. degrees in mathematics and physics from the University of California at Irvine, Irvine, CA, USA, and the Ph.D. degree in mathematics from Stony Brook University, Stony Brook, NY, USA, where he specialized in the study of differential geometry.

In 1992, he joined the staff of the Jet Propulsion Laboratory (JPL), Pasadena, CA, USA, where he is a Senior Research Scientist studying advanced radar techniques for geophysical applications. He has worked on most of the synthetic aperture radar systems developed at JPL over the past two decades, including the Magellan and Cassini radars. He was the GeoSAR Chief Scientist, a simultaneous X-band and P-band airborne radar interferometer for mapping above and beneath the canopy that is now commercially operated by Earthdata International. He leads the SRTM Interferometric Processor Development Team for a shuttle-based interferometric radar used to map the Earth's topography between 60 latitude. Recently, he began working with the Earth-based Goldstone Solar System Radar to generate topographic maps of the lunar surface. He was a Principal Investigator and is currently the Chief Scientist for the National Aeronautics and Space Administration UAVSAR Program.